Signatures of the non-Maxwellian κ-distributions in optically thin line spectra

II. Synthetic Fe XVII–XVIII X-ray coronal spectra and predictions for the Marshall Grazing-Incidence X-ray Spectrometer (MaGIXS)

Jaroslav Dudík[1],[*], Elena Dzifčáková[1], Giulio Del Zanna[2], Helen E. Mason[2], Leon L. Golub[3],
Amy R. Winebarger[4], and Sabrina L. Savage[4]

[1] Astronomical Institute, Academy of Sciences of the Czech Republic, 25165 Ondřejov, Czech Republic
   e-mail: `jaroslav.dudik@asu.cas.cz`
[2] Department of Applied Mathematics and Theoretical Physics, CMS, University of Cambridge, Wilberforce Road,
   Cambridge CB3 0WA, UK
[3] Harvard-Smithsonian Center for Astrophysics, 60 Garden Street, Cambridge, MA 01238, USA
[4] NASA Marshall Space Flight Center, Mail Code ST 13, Huntsville, AL 35812, USA

ABSTRACT

Aims. We investigated the possibility of diagnosing the degree of departure from the Maxwellian distribution using the Fe XVII–Fe XVIII spectra originating in plasmas in collisional ionization equilibrium, such as in the cores of solar active regions or microflares.
Methods. The original collision strengths for excitation are integrated over the non-Maxwellian electron κ-distributions characterized by a high-energy tail. Synthetic X-ray emission line spectra were calculated for a range of temperatures and κ. We focus on the 6–24 Å spectral range to be observed by the upcoming Marshall Grazing-Incidence X-ray Spectrometer MaGIXS.
Results. We find that many line intensity ratios are sensitive to both T and κ. Best diagnostic options are provided if a ratio involving both Fe XVII and Fe XVIII is combined with another ratio involving lines formed within a single ion. The sensitivity of such diagnostics to κ is typically a few tens of per cent. Much larger sensitivity, of about a factor of two to three, can be obtained if the Fe XVIII 93.93 Å line observed by SDO/AIA is used in conjuction with the X-ray lines.
Conclusions. We conclude that the MaGIXS instrument is well-suited for detection of departures from the Maxwellian distribution, especially in active region cores.

Key words. Sun: UV radiation – Sun: X-rays, gamma rays – Sun: corona – radiation mechanisms: non-thermal

1. Introduction

The coronal heating problem (e.g., Klimchuk 2006, 2015; Schmelz & Winebarger 2015) has been with us for many decades. Highest plasma temperatures (outside solar flares) are observed within the cores of active regions, where the temperatures reach 3 MK or more. These locations emit prominently in soft X-ray and extreme-ultraviolet (EUV) wavelengths (e.g., Parkinson 1973, 1975; Walker et al. 1974; Hutcheon et al. 1976; Bromage et al. 1977; Saba & Strong 1991; Brosius et al. 1996; Nagata et al. 2003; Reale 2010; Winebarger et al. 2011; Warren et al. 2011, 2012; Teriaca et al. 2012; Testa & Reale 2012; Del Zanna 2013a; Del Zanna & Mason 2014; Del Zanna et al. 2015a; Nuevo et al. 2015; Schmelz et al. 2015; Li et al. 2015; Brooks & Warren 2016; Ugarte-Urra et al. 2017; Parenti et al. 2017). Emission at such temperatures are also observed from stars with coronae, such as Procyon (e.g., Testa & Reale 2012), including active stars, such as Capella (e.g., Phillips et al. 2001; Desai et al. 2005; Clementson & Beiersdorfer 2013; Beiersdorfer et al. 2011, 2014), α Cen B, AB Dor, and others (e.g., Wood et al. 2018).

The emission of the solar active region cores is typically observed in spectral lines such as Fe XVI–Fe XVIII (see

Del Zanna & Mason 2018, for a recent review), or within X-ray or EUV filters such as those onboard Hinode/XRT (Golub et al. 2007) or the 94 Å channel of the Atmospheric Imaging Assembly (AIA, Lemen et al. 2012; Boerner et al. 2012) onboard Solar Dynamics Observatory. Emission originating at temperatures even higher than 3 MK can also be present, as a consequence of impulsive (nanoflare) energy release (Reale et al. 2009a,b; Schmelz et al. 2009a,b; Patsourakos & Klimchuk 2009), that likely recurs at timescales comparable to cooling timescales of individual coronal loops (e.g., Cargill 2014; Bradshaw & Viall 2016). The emission measure of plasma at such temperatures is however likely low (see, e.g., Warren et al. 2012), and in addition, the current instrumentation has a "blind spot" at higher temperatures (Winebarger et al. 2012). Upper limits to the emission at higher temperatures are provided by Del Zanna & Mason (2014) using earlier X-ray spectra from SMM/FCS and by Parenti et al. (2017) using ultraviolet SoHO/SUMER spectra.

To overcome this difficulty and to observe plasma that is typically formed in the active region cores, as well as to elucidate the properties of its heating, observations in the X-ray spectral range are needed. Such observations should be provided by the upcoming Marshall Grazing-Incidence X-ray Spectrometer (MaGIXS, Kobayashi et al. 2010, 2017, 2018).

MaGIXS is an X-ray spectrometer designed to observe the solar spectrum at 6–24 Å (0.5–2.0 keV) with a spectral resolution better than 50 mÅ near the center of a slit of ±4′ length. Its spatial resolution is about 5″. The launch of MaGIXS on a NASA sounding rocket is currently planned for spring 2020. On the basis of previous X-ray observations (cf., Parkinson 1975; Del Zanna & Mason 2014), we expect Fe xvii lines to be prominent in MaGIXS spectra. For active conditions, Fe xviii and perhaps higher ionization stages could be present. We therefore have considered here Fe xvii and Fe xviii our primary diagnostic ions. The recent atomic data and line identifications for these ions have been reviewed by Del Zanna (2006, 2011).

An additional science objective of MaGIXS is to elucidate the possible presence of departures from the equilibrium Maxwellian distribution of electrons in the plasma of active regions. The non-Maxwellians, especially in the form of high-energy tails (see review of Dudík et al. 2017a), could arise as a consequence of energy release (including impulsive heating), whether by reconnection (e.g., Cargill et al. 2012; Gordovskyy et al. 2014) including merging of magnetic islands (Drake et al. 2013; Montag et al. 2017, with the power-law tail depending on reconnection parameters); wave-particle interaction (e.g., Petrosian & Liu 2004; Laming & Lepri 2007; Vocks et al. 2008, 2016), turbulence (e.g., Hasegawa et al. 1985; Che & Goldstein 2014; Bian et al. 2014), or combination of these processes, such as excitation of waves by impulsive energy release, and subsequent non-local wave dissipation (see, e.g., Sect. 4 of Arregui 2015, for an estimate of wave dissipation timescales). Alternatively, high-energy tails arise wherever the ratio of the electron mean-free path to the pressure scale-length (the Knudsen number) is less than about 0.01 (Scudder & Karimabadi 2013), a condition that is expected to commonly occur in solar and stellar coronae. The fundamental reason for the presence of high-energy tails is the behavior of electron cross-section for Coulomb collisions, which behaves as E^{-2}, leading to the collisonal frequency τ_{coll} scaling as $E^{-3/2}$, where E is the electron kinetic energy. This means that the progressively higher-E electrons are more difficult to equilibrate. In fact, the high-energy tail can take hundreds or thousands times longer to equilibrate than the thermal core of the distribution (Galloway et al. 2010).

While non-Maxwellian distributions containing high-energy, power-law tails are routinely detected in solar wind (e.g., Marsch et al. 1982a,b; Maksimovic et al. 1997a,b; Le Chat et al. 2010, 2011), in solar flares (e.g., Seely et al. 1987; Kašparová & Karlický 2009; Veronig et al. 2010; Fletcher et al. 2011; Oka et al. 2013, 2015; Battaglia & Kontar 2013; Battaglia et al. 2015; Simões et al. 2015; Kuhar et al. 2016), and can even be present in microflares (Hannah et al. 2010) as a high-energy excess at energies of $\gtrsim$5 keV (Glesener et al. 2017; Wright et al. 2017), their detection elsewhere remains difficult. For example, only upper limits can be obtained in some microflare events in both active regions and quiet Sun (Marsh et al. 2017; Kuhar et al. 2018) even with current X-ray instrumentation such as the Nuclear Spectroscopic Telescope Array (NuSTAR, Harrison et al. 2013) and Focusing Optics X-ray Solar Imager (FOXSI, Glesener et al. 2016).

Detection of non-Maxwellians from line spectra has also been investigated, however it is non-trivial as well. To detect departures from a Maxwellian, ratios of intensities of two lines of the same ion must either have sufficiently different excitation energy tresholds or different behavior of the excitation cross-section with energy. Dudík et al. (2014) investigated the sensitivity of the EUV lines of Fe ix–Fe xiii observed by the Extreme-Ultraviolet Imaging Spectrometer (EIS, Culhane et al.

2007) onboard the Hinode satellite (Kosugi et al. 2007). It was found that a vast majority of single-ion line ratios show almost no sensitivity to the non-Maxwellian κ-distributions (e.g., Owocki & Scudder 1983; Livadiotis & McComas 2009; Livadiotis 2015, 2017), even for strong non-thermal tails (i.e., low κ). This comes from the fact that most EIS lines of Fe ix–Fe xiii have similar wavelengths and are formed from similar energy levels. The temperature-sensitive ratios were an exception, showing a sensitivity on the order of several tens of per cent (Dudík et al. 2014). Typically, such ratios involved one line from the short-wavelength channel, while the other was from the long-wavelength channel of EIS. Such ratios, in combination with ratios involving lines from neighboring ionization stages, were subsequently used by Dudík et al. (2015) to detect indications of strong departures from a Maxwellian ($\kappa \lesssim 2$) in a transient coronal loop. However, such analysis is complicated by the different in-flight degradation of the two EIS wavelength channels (Del Zanna 2013b). Dzifčáková et al. (2018) used the line ratios of Fe xviii–Fe xix and Fe xxi–Fe xxii observed by the Extreme-Ultraviolet Experiment (EVE, Woods et al. 2012) onboard the SDO during an X-class flare. Lines formed at widely different wavelengths were available for diagnostics, and the results showed strong departures ($\kappa \lesssim 2$) from the Maxwellian in the early and impulsive phase of the flare, with subsequent Maxwellianization toward the peak and gradual phases of the flare. Finally, indications of strongly non-Maxwellian distributions were found from the profiles as well as intensities of the transition region lines (Dudík et al. 2017b) observed by the Interface Region Imaging Spectrograph (IRIS, De Pontieu et al. 2014). Non-Maxwellian line profiles were also detected from EIS observations of coronal holes (Jeffrey et al. 2018) and flares (Polito et al. 2018).

The 6–24 Å passband of MaGIXS contains numerous Fe xvii and Fe xviii lines, which are the focus of this study. These lines originate in both active region cores and microflares, while the passband of MaGIXS could contain unexplored possibilities for the detection of non-Maxwellian distributions. In addition, the Fe xviii 93.93 Å line observed by AIA, widely separated in wavelength from the MaGIXS passband, can be utilized to increase the sensitivity to both temperature and the non-Maxwellians. This work is organized as follows. The non-Maxwellian κ-distributions are described in Sect. 2. The method for calculations of synthetic spectra are detailed in Sect. 3, while the results are given in Sect. 4. A summary is given in Sect. 5. Finally, the Appendix A provides details on the transitions (spectral lines) investigated, together with their blends and self-blends.

2. The non-Maxwellian κ-distributions

The κ-distribution (Fig. 1, left) is a distribution of electron velocities or energies, containing a characteristic power-law high-energy tail (Owocki & Scudder 1983; Livadiotis & McComas 2009). In its isotropic energy form, the expression for a κ-distribution is (see, e.g., Livadiotis 2015, as well as Livadiotis 2017, chapter 4.3.1.3.2 therein)

$$f(E, \kappa)dE = A_\kappa \frac{2}{\sqrt{\pi}(k_B T)^{3/2}} \frac{E^{1/2}dE}{\left(1 + \frac{E}{(\kappa - 3/2)k_B T}\right)^{\kappa+1}}, \quad (1)$$

where E is electron kinetic energy and $k_B = 1.38 \times 10^{-16}$ erg K^{-1} is the Boltzmann constant. The distribution is normalized to unity via

$$A_\kappa = \frac{\Gamma(\kappa + 1)}{\Gamma(\kappa - 1/2)(\kappa - 3/2)^{3/2}}. \quad (2)$$
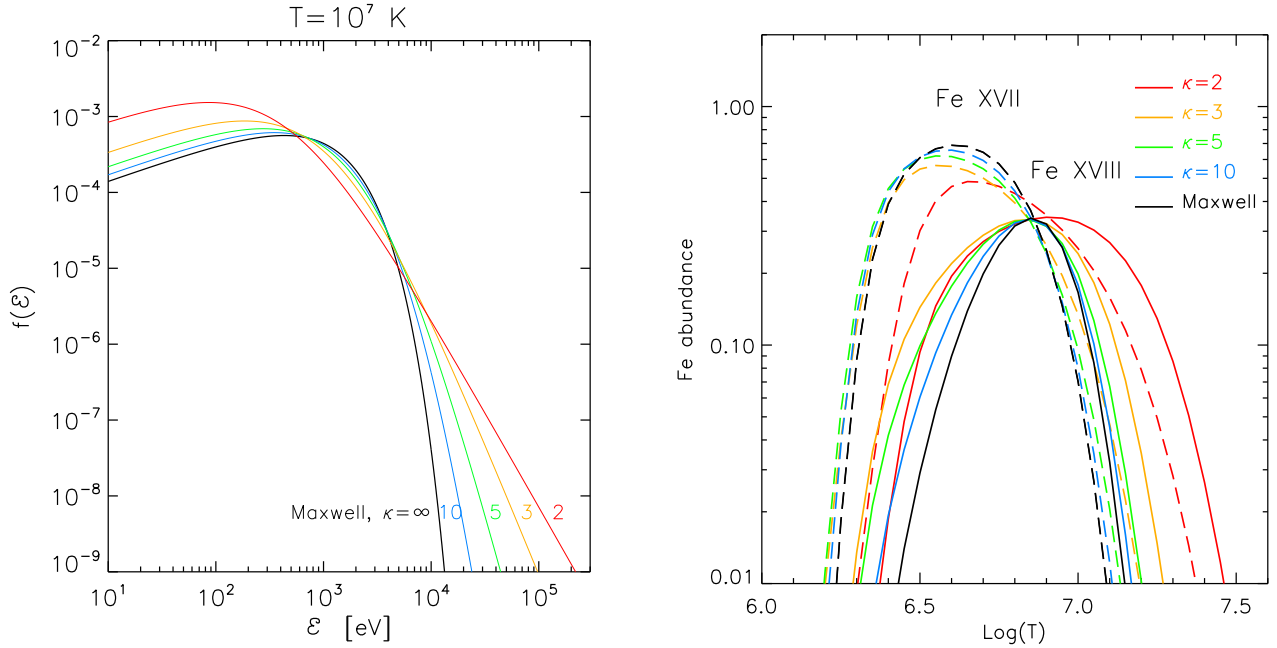
Fig. 1. *Left*: electron κ-distribution as a function of electron kinetic energy E. *Right*: relative abundances of the Fe XVII (dashed lines) and Fe XVII (full lines). Different colors correspond to different distributions.

The κ-distribution has two independent parameters (thermodynamic indices), T and κ, see, for example, Livadiotis (2015, 2017). The T is the thermodynamic temperature (see also Livadiotis & McComas 2009), coinciding with the definition in mean energy of the distribution $\langle E \rangle = 3k_BT/2$. The parameter $\kappa \in (3/2, +\infty)$ describes the deviation from the Maxwellian. Maxwellian distribution is recovered for $\kappa \to \infty$, while $\kappa \to 3/2$ represents the asymptotic, extremely non-Maxwellian situation.

We note that the κ-distribution can be thought of as consisting of a near-Maxwellian core and a high-energy power-law tail (Oka et al. 2013). While the slope of the high-energy tail is given by $-(\kappa + 1/2)$, the low-energy end of the distribution can be well approximated by a Maxwellian with a temperature $T_M = T(\kappa - 3/2)/(\kappa + 1)$ (Meyer-Vernet et al. 1995; Livadiotis & McComas 2009). This permitted Oka et al. (2013) to calculate the relative number of the particles in the high-energy tail, as well as the energy carried by these particles. For example, for a moderately non-Maxwellian situation of $\kappa = 5$, the high-energy tail contains $\approx 16\%$ of particles carrying $\approx 42\%$ of energy. For a more extreme $\kappa = 2$ situation, the high-energy tail contains $\approx 36\%$ particles carrying more than 83% of total kinetic energy of the distribution (Fig. 1b of Oka et al. 2013).

3. Spectral synthesis

3.1. Spectral line emissivities

The spectral synthesis of optically thin Fe XVII and Fe XVIII lines here is done analogously to Dudík et al. (2014, hereafter, Paper I). The intensity I_{ji} of a spectral line corresponding to a transition $j \to i$ between levels $j > i$ is given by (cf., Mason & Monsignori Fossi 1994; Phillips et al. 2008)

$$I_{ji} = \int A_X G_{X,ji}(T, N_e, \kappa) N_e N_H dl, \tag{3}$$

where l is the line of sight, N_e and N_H are the electron and hydrogen densities, respectively, A_X is the abundance of element X,

and $G_{X,ji}(T, N_e, \kappa)$ is the line contribution function, given by the expression

$$G_{X,ji}(T, N_e, \kappa) = \frac{hc}{\lambda_{ji}} \frac{A_{ji}}{N_e} \frac{N(X_j^{+k})}{N(X^{+k})} \frac{N(X^{+k})}{N(X)}. \tag{4}$$

There, λ_{ji} is the line wavelength, hc/λ_{ji} is the corresponding photon energy, A_{ji} is the Einstein coefficient for the spontaneous emission, $N(X_j^{+k})/N(X^{+k})$ is the fraction of the ion X^{+k} with the electron on the upper excited level j, and $N(X^{+k})/N(X)$ is the relative ion abundance of the ion X^{+k}.

3.2. Ionization and excitation equilibria for the κ-distributions

Both the relative ion abundance $N(X^{+k})/N(X)$ and the excitation fraction $N(X_j^{+k})/N(X^{+k})$ are functions of κ. This comes from the fact that the individual ionization, recombination, excitation, and deexcitation rates all depend on κ (e.g., Dzifčáková & Dudík 2013; Dudík et al. 2014; Dzifčáková et al. 2015, and references therein). These ratios were calculated by assuming ionization and excitation equilibrium, respectively, in other words, these fractions were assumed to be time-independent. For the excitation equilibrium, this assumption is justified since the equilibration times are small, depending on the corresponding A_{ji} values and the excitation rates C_{ij}^e. At densities of $\log(N_e \, [\text{cm}^{-3}]) = 10$, the $N_e C_{ij}^e$ is on the order of 0.1–$1 \, \text{s}^{-1}$ for allowed lines of Fe XVII and Fe XVIII at $\log(T \, [\text{K}]) = 6.6$ (e.g., Fig. 2), that is, temperatures typical of an active region cores.

The ionization equilibration timescales can however be larger. For iron, they are on the order of ten seconds at $\log(T \, [\text{K}]) = 6.6$, according to Fig. 1 of Smith & Hughes (2010). These results were calculated for the Maxwellian distribution; however, the ionization equilibration timescales will not be significantly different for the κ-distributions at these temperatures, since the ionization and recombination rates for κ-distributions do not differ by more than about a half an order of magnitude at $\log(T \, [\text{K}]) = 6.6$ (see Fig. 2 of Dzifčáková & Dudík 2013),
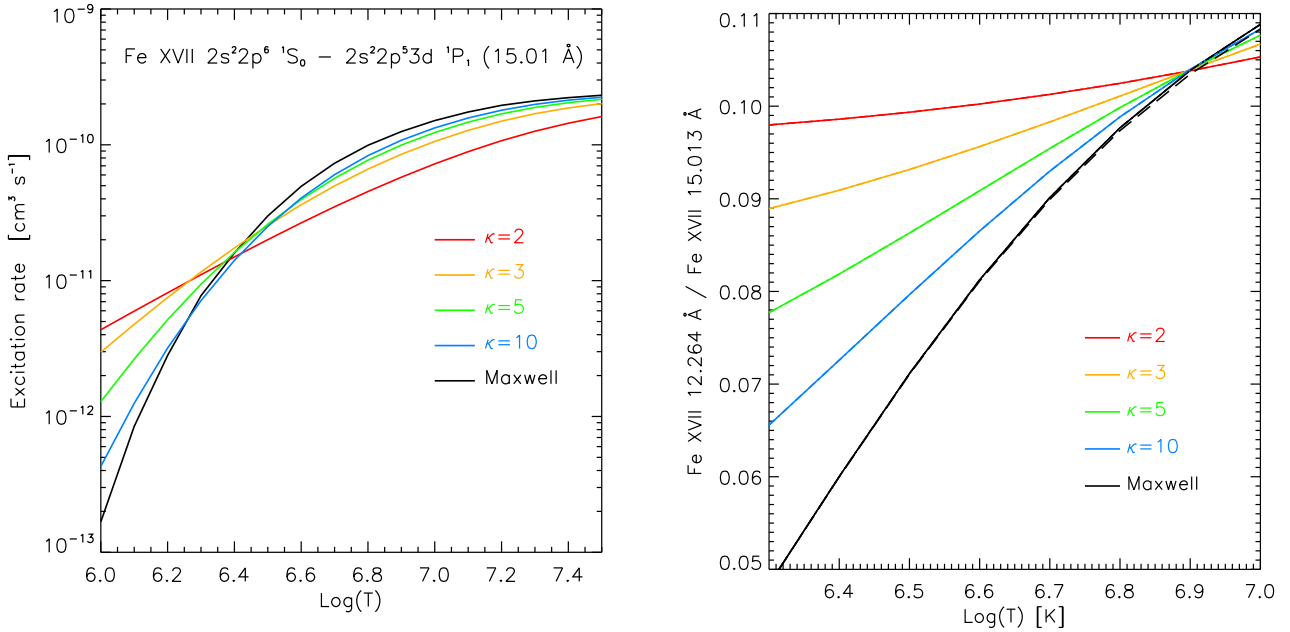
Fig. 2. *Left*: effect of the electron distribution on the excitation rate of Fe xvii line 15.01 Å. *Right*: changes of the line intensity ratios with the electron distribution for the Fe xvii 15.01 Å/12.25 Å. The line ratios are not density dependent.

with the ionization rates increasing for lower κ compared to a Maxwellian.

Therefore, the results obtained in this paper are valid for active region cores that do not display significant temporal variability on the order of ten seconds or less.

Finally, the relative ion abundance of Fe xvii and Fe xviii obtained by Dzifčáková & Dudík (2013) are shown in Fig. 1. There, the dashed and full lines stand for Fe xvii and Fe xviii, respectively, while the different colors denote different values of κ. The typical widening of the peaks of the relative ion abundances for lower κ is evident. Furthermore, for $\kappa \lesssim 2$, a shift of the peaks to higher T occurs. This shift is only about 0.05 in $\log(T \, [\mathrm{K}])$ for both Fe xvii and Fe xviii (Fig. 1). The atomic data behind the individual ionization and recombination rates correspond to CHIANTI database, versions 6–8 (Dere et al. 1997, 2009; Dere 2007; Landi et al. 2013; Del Zanna et al. 2015b).

The collisional excitation and de-excitation rates were calculated by direct integration of the original collision strengths Ω_{ji} (non-dimensionalized excitation cross-sections) over the κ-distributions using the method of Bryans (2006), described in detail in Paper I (see Eqs. (4)–(16) therein).

The collision strengths Ω_{ji} as well as the A_{ji} values were calculated by Liang & Badnell (2010) for Fe xvii and Del Zanna (2006) for Fe xviii. We note that these atomic data are also consistent with CHIANTI, version 8.0.7 (Dere et al. 1997; Del Zanna et al. 2015b).

3.3. Corrections to level populations due to ionization and recombination

The line emissivity calculations outlined in previous sections were done in the coronal approximation. This means that the populations of the excited levels of the Fe xvii and Fe xviii are negligible compared to the population of the ground level. This means that the ionization and recombination happens dominantly from and to the ground level, respectively. However, this approximation does not always hold for Fe xvii (Doron & Behar 2002) as well as for higher ionization states of Fe (Gu 2003).

Doron & Behar (2002) calculated the Fe xvii emissivities by including the neighboring ionization stages of Fe xvi and Fe xviii, while assuming that their relative ion abundances are imposed. These authors showed that some strong lines of Fe xvii, such as the 2p–3s at 16.78, 17.05, and 17.10 Å (see Appendix A) contain significant contributions, exceeding 50% in some cases, from resonant excitation and dielectronic recombination. The resonant excitation is dominant at coronal temperatures, while the importance of dielectronic recombination increases with increasing temperatures, when the relative abundance of Fe xvii is small compared to Fe xviii (see also Fig. 1). Contrary to that, the contribution of the inner-shell ionization changes the level populations by less than about 3%. Gu (2003) extended these results to Fe xvii–Fe xxiv, while providing tabulated values of the rates of individual processes.

In the CHIANTI atomic database and software, the contributions of resonant excitation for Fe xvii and Fe xviii is already included in the electron excitation rates, since these are based on the collision strengths Ω_{ji} which themselves contain the resonances. The contributions to the level populations from level-resolved dielectronic recombination and collisional ionization are included via the correction factors (see Eq. (10) of Landi et al. 2006) that are based on the ionization and recombination rates of Gu (2003) and are applied to the level populations calculated in coronal approximation.

We note that Gu (2003) calculated the level-resolved ionization and recombination rates for the Maxwellian distribution. Furthermore, these rates are effective since they include the contribution of cascading. For this reason, the corresponding non-Maxwellian rates cannot be easily calculated using the method of Dzifčáková & Dudík (2013). This is because the contribution of cascading cannot be separated from the ionization and recombination to upper levels. In addition, Gu (2003) included many upper levels (up to $n = 45$ compared to only levels up to $n = 6$ in CHIANTI). Therefore, including level-resolved ionization and recombination to $n \leq 6$ levels for non-Maxwellians would still not contain the contributions from cascading from higher levels. Work is however ongoing in this respect (Dzifčáková et al., in prep.).
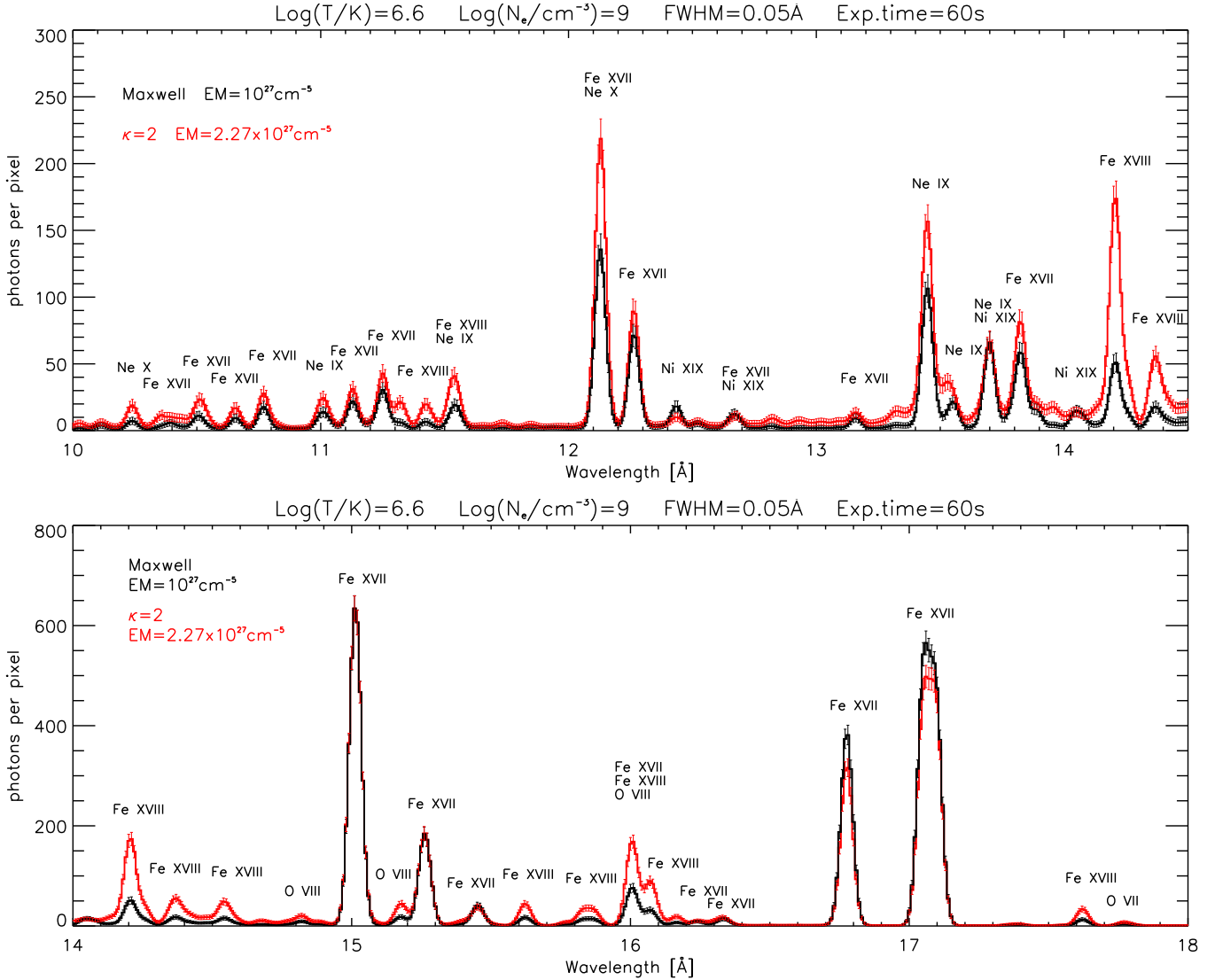
Fig. 3. Example synthetic MaGIXS spectra at 10–18 Å. The Maxwellian spectrum (black) is compared here with a spectrum obtained for $\kappa = 2$ (red). Both spectra were calculated for $\log(T \text{ [K]}) = 6.6$ and $N_\mathrm{e} = 10^9 \text{ cm}^{-3}$. Error-bars indicate photon noise uncertainty in a 60 s integration time. The assumed FWHM of the lines is 0.05 Å. Principal ions forming a particular spectral line are indicated. For details on blends see Appendix A.

For the above reason, we calculated the level populations for non-Maxwellians without the correction factors. For the Maxwellian distribution, the corresponding error created by not including the correction factors is always less than about 8% in Fe XVII X-ray line intensities at temperatures $\log(T \text{ [K]}) \leq 6.6$, with only some lines being affected (see, e.g., Doron & Behar 2002; Gu 2003). For the Fe XVIII, the X-ray line intensities change by $\lesssim 9\%$, with the lines 15.83–16.07 Å being the most affected. Notably, the 93.93 Å line is affected by only about 2% at these temperatures. In this respect, at coronal temperatures, the corrections to level populations due to ionization and recombination are secondary effects, as also noted by Del Zanna (2011). Nevertheless, to indicate the influence of these corrections for the Maxwellian distribution, the corresponding ratios of line intensities calculated with the correction factors are shown by dashed black lines in Figs. 4–7. We note that the contributions from dielectronic recombination increase with increasing temperature. Therefore, some ratios can become less reliable for diagnostics of non-Maxwellian distributions in case of high-temperature plasma, for example in flares. Details for respective cases are provided in Sect. 4.2.

4. Results

4.1. Synthetic MaGIXS line spectra

We calculated the synthetic spectra of Fe XVII–Fe XVIII using the method outlined in Sect. 3. In addition, lines of other ions and elements (such as Ne IX, Ni XIX, and O VIII) producing lines in the MaGIXS spectral window were calculated using the KAPPA database (Dzifčáková et al. 2015). The synthetic MaGIXS spectra are shown in Fig. 3. These are example spectra, calculated in isothermal conditions for $\log(T \text{ [K]}) = 6.6$, assuming the Maxwellian (black) as well as the κ-distribution with $\kappa = 2$ (red color). The spectra were calculated in the range of 10–18 Å, where many prominent Fe XVII and Fe XVIII lines are present (see also Appendix A). The line intensities were calculated in photon units (phot cm^{-2} s^{-1} sr^{-1}), then converted to counts based on the MaGIXS effective area as a function of wavelength, assuming pixel size and slit width of 2″5, integration time of 60 s, and emission measure $EM = 10^{27}$ cm^{-5} typical of small active regions (Warren et al. 2012, Figs. 1 and 6 therein). Finally, the spectra were convolved with Gaussian line profiles using a constant FWHM of 0.05 Å (with pixel size of 0.01 Å). Photon noise

uncertainties are indicated by error-bars. The read noise was not added as it is expected to be significantly smaller than the photon noise. Finally the emission measure for the spectrum with $\kappa = 2$ was multiplied by a factor of 2.27 so that the line intensity ratio of the Fe XVII 15.01 Å/15.26 Å lines is the same for both Maxwellian and a κ-distribution. In this way, the changes in line intensities for $\kappa = 2$ with respect to the Maxwellian should become readily apparent.

From the synthetic spectra shown in Fig. 3 it is apparent that some lines are quite sensitive to the κ-distributions. The strong Fe XVII $2p^6 - 2p^53s$ lines at 16.78 Å, and the 17.05 and 17.09 Å selfblend are decreased for the $\kappa = 2$. Largest differences however occur for weaker lines of both Fe XVII and Fe XVIII, many of which however have less than about 5% intensity relative to Fe XVII 15.01 Å. Detailed diagnostics using these lines are given in Sect. 4.2. To further show the changes with κ in these weaker lines, as well as their photon noise uncertainties, the spectrum of Fig. 3 is also plotted in Appendix B using a logarithmic intensity scale.

Other conspicuous examples of lines sensitive to κ-distributions include the He-like Ne IX lines at 13.55 and 13.71 Å, which are however not dealt with in this paper. This is since the Ne IX lines are not sufficiently numerous to construct a reliable diagnostics of κ in the same manner as is done for Fe XVII and Fe XVIII in Sect. 4.2. We also note that the He-like Ne IX lines are sensitive to excitation, which significantly increases their formation temperature compared to the peak of the relative ion abundance. For Maxwellian, the lines are formed at about $\log(T\,[\mathrm{K}]) = 6.6$, while the broad peak of the relative ion abundance is at $\log(T\,[\mathrm{K}]) = 6.25$. For $\kappa = 2$, the shift is to $\log(T\,[\mathrm{K}]) = 6.5$ instead of ≈ 6.1.

4.2. Theoretical diagnostics

In the following, we investigate the possible diagnostics of non-Maxwellians using the ratio–ratio diagrams (Dudík et al. 2014, 2015; Dzifčáková et al. 2018). The ratio–ratio diagrams plot the dependence on one line intensity ratio on another line intensity ratio. Typically, one ratio is chosen to be dominantly sensitive to temperature, while the other is sensitive to κ. Such ratios involve lines separated in wavelength, that is, with different excitation tresholds; and thus sensitive to different parts of the electron energy distribution. Alternatively, a ratio is sensitive to κ if the behavior of the collision strengths Ω_{ji} with energy for the two lines are different. In practice, both ratios in a ratio–ratio diagram are sensitive to both T and κ to some degree, since both T and κ are independent parameters of the κ-distribution (see Eq. (1)).

We used both single-ion ratios as well as combinations of Fe XVII and Fe XVIII lines. The list of spectral lines investigated is provided in Appendix A together with their blends and selfblends. We note that many of the lines are blended (Tables A.1 and A.2), with the importance of some blends, such as those of Fe XIX, being dependent on the conditions (cf., Hutcheon et al. 1976).

We also note that the Fe XVII is not sensitive to electron density, as noted already by Loulergue & Nussbaumer (1975). This holds to large electron densities, of about $10^{11}\,\mathrm{cm}^{-3}$, as also noted by Del Zanna (2011). Above $10^{11}\,\mathrm{cm}^{-3}$, some Fe XVII lines can become density-sensitive, for example, the 17.09 Å line decreases in intensity with respect to the neighboring 17.05 Å one (e.g., Phillips et al. 2001). The Fe XVIII is similarly not very sensitive to N_e in the low-density limit relevant for solar corona and flares (Del Zanna 2006). The validity of this fact can be

discerned directly from Figs. 4–7, where the dash-dotted lines stand for $N_e = 10^{11}\,\mathrm{cm}^{-3}$, while the full lines denote the spectra calculated for $N_e = 10^9\,\mathrm{cm}^{-3}$. The difference between the two is very small or indeed not recognizable.

4.2.1. Single-ion diagnostics

We first investigated ratios of lines originating with only a single ion. This has the advantage of not being strongly sensitive to departures from ionization equilibrium (Dudík et al. 2014); although in principle some sensitivity could arise due to the contribution of dielectronic recombination to upper excited levels. However, we focused on lines for which the correction factors (Sect. 3.3) are negligible at coronal temperatures. To illustrate the influence of the ionization from and recombination to the excited levels for the Maxwellian distribution, a black dashed line is plotted in Figs. 4–7. Compared to that, the full black line stands for the Maxwellian spectra without the correction factors. Finally, the colored lines denote individual values of κ, where we consider $\kappa = 10, 5, 3,$ and 2, respectively.

Unlike in EUV (Dzifčáková & Del Zanna 2012), the diagnostic possibilities using only the lines of Fe XVII are limited. This is primarily due to the fact that the Fe XVII lines occur only at wavelengths of 10–18 Å, and all transitions are to the ground state (Table A.1). Most of the line intensity ratios have only a restricted range for $\kappa = 2$ compared to the Maxwellian. An example is shown in the left panel of Fig. 4. Despite the seeming spread of the ratio–ratio curves for different κ, the Fe XVII 13.82 Å+13.89 Å/12.26 Å displays only about $\approx 4\%$ sensitivity to κ. This is too low for a reliable detection, given the likely photon noise uncertainties in these weak Fe XVII lines. The conjugate ratio of Fe XVII 12.26 Å/11.25 Å is however limited to values of about 2.2 (in photon units) for $\kappa = 2$, compared to a much larger range of 2.15–2.60 for the Maxwellian distribution and temperatures of $\log(T\,[\mathrm{K}]) = 6.4$–7.0. Therefore, a measurement of this ratio of about 2.2 could be a potential indicator of $\kappa \approx 2$.

Ratios of weak Fe XVII lines with respect to the stronger lines, such as those at 15.01 and 15.26 Å, do show sensitivity to κ. An example is shown in the right panel of Fig. 4, where the Fe XVII 15.26/12.26 Å ratio is combined with the ratio of the Fe XVII 15.26 Å to the blend of Fe XVII+Fe XVIII at 15.45 Å. Although the latter ratio involves both Fe XVII and Fe XVIII, at temperatures below $\log(T\,[\mathrm{K}]) \le 6.6$ (6.8), about 95% (75%) of the intensity of the blend is due to a single transition within Fe XVII. In this ratio–ratio diagram, the sensitivity to κ increases toward the lower temperatures, a feature typical of single-ion ratios (cf., Figs. 8–10 of Paper I). Such increase occurs because even for a low temperature, a κ-distribution with low κ still has many high-energy electrons for the excitation to occur. This is advantageous for detection of non-Maxwellians in the plasma of active region cores.

We note that the 12.26, 15.26, and 15.45 Å lines were well-observed by Parkinson (1975) using the KAP (potassium-acid-phtalate) crystal. After transforming the intensities listed in Table 1 therein to photon units, we obtain a value of ≈ 3.0 for the Fe XVII 15.26 Å/15.45 Å ratio. The conjugate Fe XVII ratio of 15.26 Å/12.26 Å reaches a value of ≈ 7.5, outside of the range shown in the right panel of Fig. 4. Such measured ratios would indicate Maxwellian plasma at low temperatures of $\log(T\,[\mathrm{K}]) \lesssim 6.3$.

Finally, we note that the 15.26 Å/12.26 Å ratio contains contributions from level-resolved ionization and recombination (Sect. 3.3), which can become important at higher temperatures, see the black dashed line in the right panel of Fig. 4. Since we
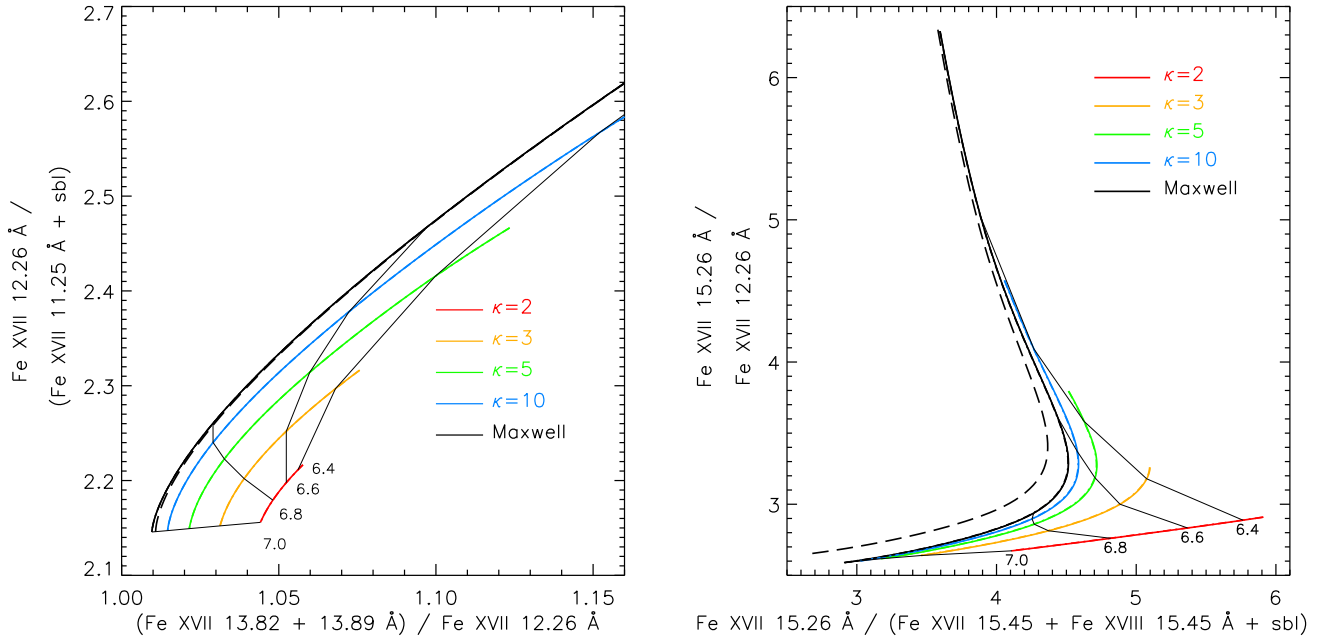
Fig. 4. Diagnostics of κ and temperature from Fe XVII from the MaGIXS spectra. Ratios of line intensities (in photon units) are indicated, with wavelengths of the lines involved listed together with the main self-blends. Individual colors denote the distribution, with black for Maxwellian, and blue, green, orange, and red for κ-distribution with $\kappa = 10$, 5, 3, and 2, respectively. Full lines correspond to spectra with for $N_e = 10^9$ cm^{-3}, while the dot-dashed lines correspond to $N_e = 10^{11}$ cm^{-3}. Black long-dashed lines (available only for the Maxwellian distribution) show the effects of the recombination and ionization to and from the upper excited levels, together with cascades. See Sect. 3.3 for more details.

are not taking these effects into account, the measured κ-value for such high temperatures will likely only be an upper limit.

The Fe XVIII produces more lines than Fe XVII in the wavelength range observed by MaGIXS. However, many of these lines are weak compared to the strong Fe XVII lines at 15.01 and 17.05 Å if the temperatures are $\log(T\,[\mathrm{K}]) = 6.6$ typical of active region cores (Fig. 3 and Table A.2). Indeed, Parkinson (1975) did not observe many of the Fe XVIII lines. In addition to blends, many of the Fe XVIII lines are self-blended by multiple Fe XVIII transitions (see Table A.2), which can have implications for their widths. Care must thus be exercised in interpreting the intensities of such lines, if observed.

We investigated combinations of the Fe XVIII line ratios for sensitivity to κ and T. Similarly to the Fe XVII, only very weakly sensitive ratios were found, with sensitivities on the order of less than about 5%. An exception are the ratios involving the 11.42 Å selfblend, which is blended with a Fe XVII transition at 11.420 Å. It is the presence of this blend that creates the sensitivity to both κ and T, which occurs at low temperatures, $\log(T\,[\mathrm{K}]) \lesssim 6.7$ (Fig. 5). In fact, the Fe XVII blend dominates the line at temperatures below $\log(T\,[\mathrm{K}]) \lesssim 6.5$. Thus, the ratio–ratio diagrams shown in Fig. 5 involving the 11.42 Å line are no longer single-ion ratios, but involve both Fe XVII and Fe XVIII, that is, the ionization equilibrium via the relative ion abundances.

4.2.2. Diagnostics involving ionization equilibrium

The combination of Fe XVII lines with one Fe XVIII line (or vice versa) provides an advantage of utilizing the ionization equilibrium, which is strongly sensitive to temperature, but also sensitive and κ (Fig. 1, right panel). This ratio of two lines formed in neighboring ionization stages can be combined with another ratio sensitive to T or κ, leading to a significant increase of sensitivity to departures from the Maxwellian distribution. We note that there are many line ratios available within Fe XVII and

Fe XVIII to measure the temperature (Del Zanna 2006, 2011), although these measurements have been performed so far only under the assumption of a Maxwellian distribution.

Before proceeding to investigate the suitable ratios for simultaneous diagnostics of T and κ, we caution again that using the ratio–ratio technique involving lines from two neighboring ionization stages can be misleading if the ionization is out of equilibrium, meaning that the relative ion abundances are time-dependent and do not correspond to those shown in Fig. 1. Thus, as already noted in Sect. 3.2, the diagnostics involving lines from neighboring ionization stages should not be applied if the observed line intensities change on timescales on the order of ≈ 10 s or less.

Since almost any line intensity ratio involving both Fe XVII and Fe XVIII is sensitive to T and κ, strong lines should be preferentially used to minimize the photon noise uncertainty in the measurements. The strongest lines of Fe XVIII at 14.20 Å, (15.83 Å+15.87 Å), 16.07 Å, and 17.62 Å are recommended. At $\log(T\,[\mathrm{K}]) = 6.6$, these Fe XVIII lines are weak compared to Fe XVII, having intensities of about 2–10% relative to the Fe XVII 15.01 Å, depending on the conditions. Nevertheless, these lines should still be measurable, and we note that the Fe XVIII lines at 14.20 Å and 17.62 Å will have increased intensities for the non-Maxwellians (see Fig. 3 and Table A.2).

With the exception of 17.62 Å, the lines of Fe XVIII at 14.20 Å, 14.37 Å, 14.54 Å, 15.62 Å, (15.83 Å+ 15.87 Å), 16.07 Å, and 16.17 Å are self-blends. The Fe XVIII 14.20 Å line is self-blended (hereafter also "sbl") with a single 14.21 Å transition (Table A.2), which contributes about 38% to the total intensity of the self-blend. The 14.37 Å and 14.54 Å lines both have many self-blends (Table A.2), some of which can contribute tens of per cent to the total intensity. The strongest self-blending transition is 14.55 Å, which contributes up to ≈ 30% to the total intensity of the 14.54 Å line. The 15.62 Å line is self-blended with two transitions at 15.62 and 15.64 Å (Table A.2), which however
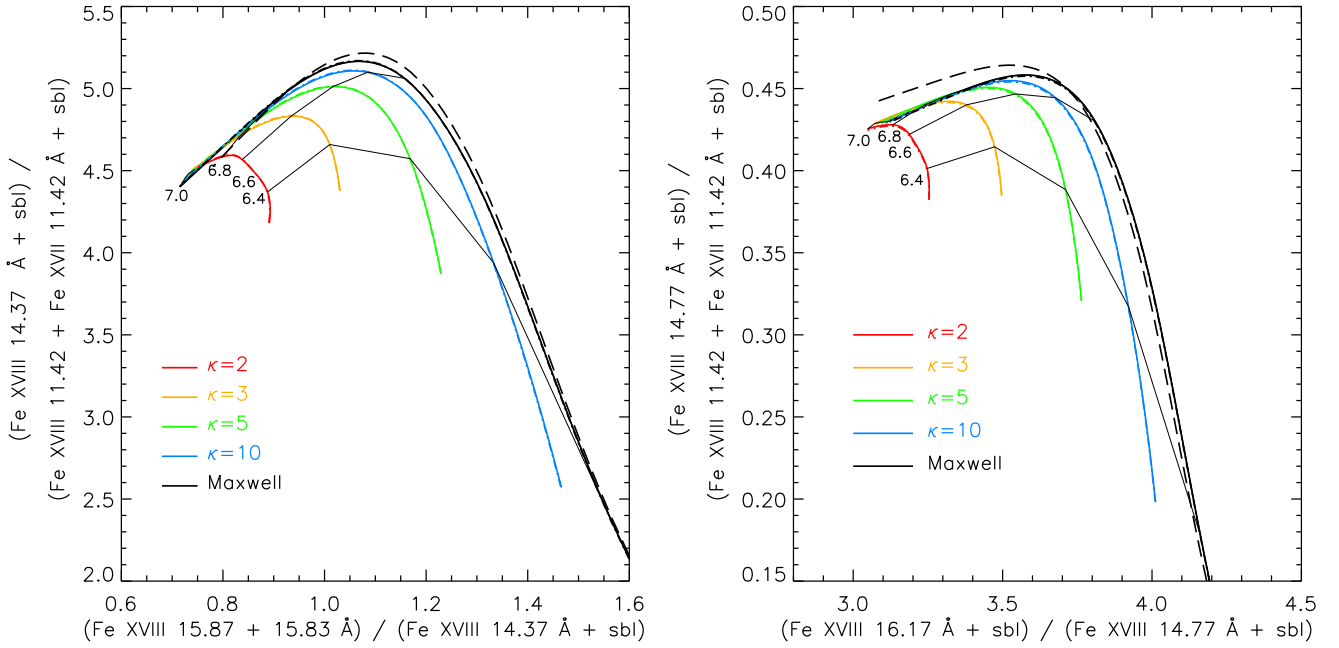
Fig. 5. Same as in Fig. 4, but for Fe xviii.

contribute less than about 1% to the total intensity. The 15.87 Å line is self-blended with another 15.87 Å transition, which contributes about 40% to the total intensity. The 15.87 Å sbl can be further self-blended at MaGIXS resolution with another transition at 15.83 Å (Table A.2). In the remainder of this Section, we sum these two lines together unless otherwise indicated. At MaGIXS resolution, the 16.07 Å line is located in the red wing of an O viii+Fe xvii blend at 16.00 Å (see Fig. B.1). This line is self-blended with a 16.09 Å transition, which contributes about 9% to the total intensity of the self-blend. We note that if hotter temperatures are present, this line can be further blended with a Fe xix transition at 16.11 Å. Finally, the 16.17 Å line is self-blended with a 16.19 Å transition, which contributes only about 1% to the total intensity. We note that depending on conditions, perhaps not all of these lines will be reliably measured, especially if shorter integration times are analyzed. Therefore, in the remainder of this work, where Fe xviii X-ray lines are concerned, we focus on diagnostics using the strongest lines, such as those at 14.20 Å, (15.83 Å+15.87 Å), 16.07 Å, and 17.62 Å. Other Fe xviii lines could however also be used for consistency checks.

Examples of diagnostic ratio–ratio diagrams using combinations of lines of both Fe xvii and Fe xviii are given in Fig. 6. There, the Fe xviii lines are used in combination with the strong lines of Fe xvii, such as those at 12.26 Å, 15.01 Å, 15.26 Å, and 16.78 Å. We note that the 17.05 Å and 17.09 Å lines, which are formed from a $3s$ upper level, can be used instead of 16.78 Å without a significant change in the shape of the ratio–ratio diagrams. However, the 17.05 and 17.09 Å lines contain larger contribution from correction factors (Sect. 3.3); therefore, the use of 16.78 Å line, although a weaker one, is recommended instead. The effect of correction factors is such that the measured value of κ will likely be an upper limit once the level-resolved dielectronic recombination is taken into account.

All ratio–ratio diagrams shown in Fig. 6, involving both Fe xvii and Fe xviii lines observable by MaGIXS, have sufficient sensitivity to κ, on the order of 20%, for the diagnostics to be feasible. Again, the sensitivity to κ is increased at lower T, which is advantageous for studying the presence of non-Maxwellians in the active region cores. The best available diagnostics is the Fe xvii 15.26 Å/Fe xviii 17.62 Å, strongly sensitive to T. This ratio can be combined for example with the Fe xviii ratio 17.62 Å/14.20 Å sbl, which is mainly sensitive to κ at low temperatures (Fig. 6). At $\log(T\,[\mathrm{K}]) \lesssim 6.6$, the latter ratio reaches a value of ≈ 0.31 for $\kappa = 2$ compared to ≈ 0.39 for a Maxwellian.

In the other ratio–ratio diagrams shown in Fig. 6, the sensitivity to κ is chiefly provided by the Fe xvii ratios such as 15.26 Å/12.26 Å, 15.45 Å (bl Fe xviii)/12.26 Å, or 16.78 Å/15.01 Å. These ratios are combined with the ratios involving both Fe xvii and Fe xviii, such as Fe xvii 12.26 Å/Fe xviii 16.07 Å sbl, Fe xvii 15.01 Å/Fe xviii 16.07 Å sbl, or Fe xvii 16.78 Å/15.45 Å (bl Fe xviii). The last case has an added complication such that the Fe xvii blend with Fe xviii at 15.45 Å creates a non-monotonous dependence on T for $\kappa \gtrsim 3$ (Fig. 6, bottom right).

Since these ratio–ratio diagrams involve only MaGIXS lines, observed within a single spectral passband of a single instrument, the precision of the diagnostics will be essentially limited by the photon noise and dark current. This a step forward from the former applications of the ratio–ratio diagnostic technique, which involved multiple spectral channels, thereby adding the uncertainty of the absolute calibration of each channel and their degradation over time; see Sect. 4.1 of Dudík et al. (2015) and Sect. 4 of Dzifčáková et al. (2018). To take advantage of the photon-noise limited diagnostics, we suggest that the uncertainty in the photon noise should be limited to about 5–10% for all lines. Since the instrument is likely to observe an active region core, this 5–10% limit in photon noise uncertainty should be applied to the Fe xviii lines, which are weaker under conditions typical of an active region core (cf., Fig. 3).

4.2.3. Diagnostics involving the Fe xviii 93.93 Å line

An increase in sensitivity to κ can be obtained if the Fe xviii 93.93 Å line is used together with the X-ray lines in the ratio–ratio diagrams. Although this well-known line will not observed by MaGIXS, it will be simultaneously observed by the SDO/AIA
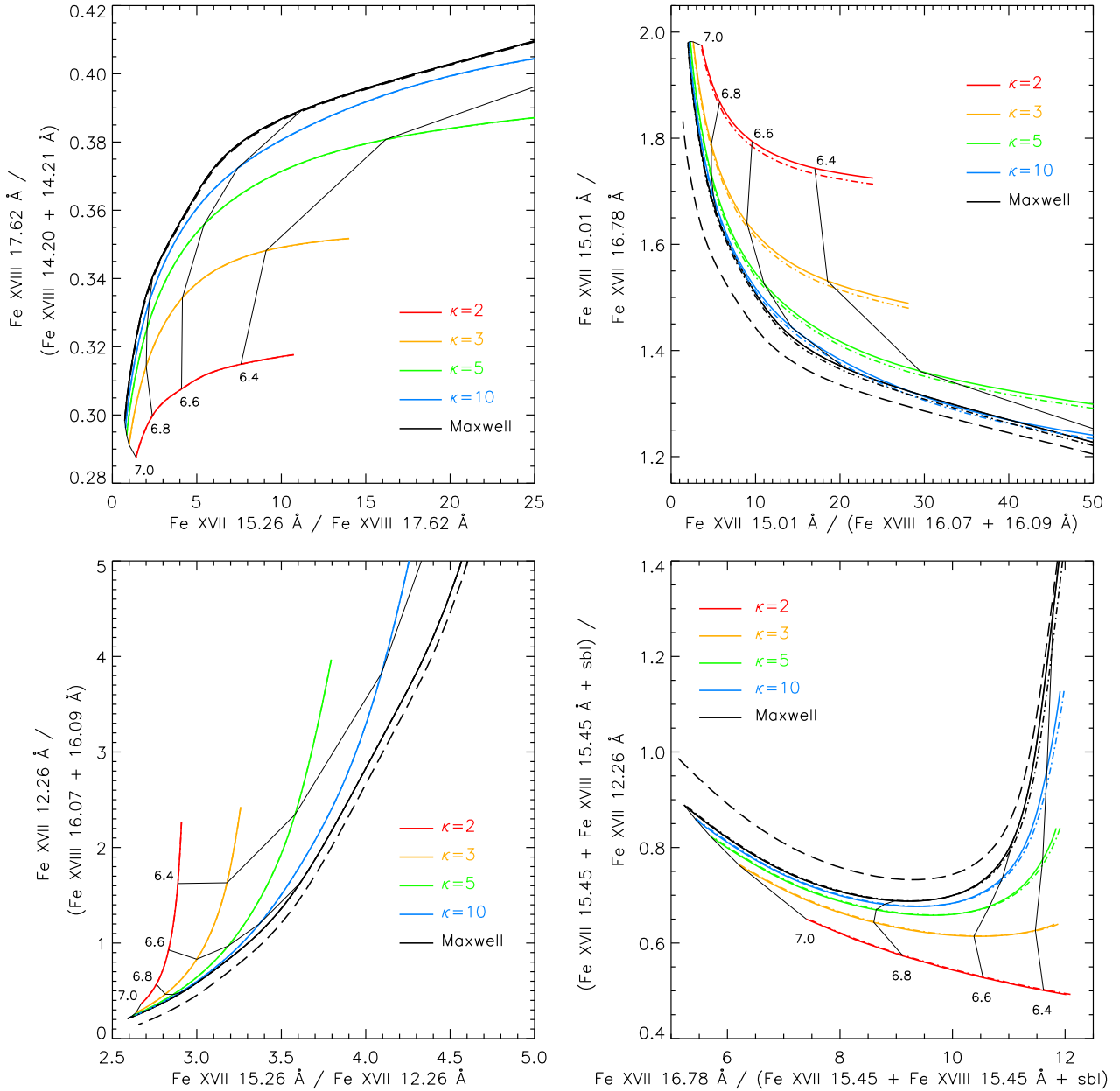
Fig. 6. Same as Fig. 4, but for diagnostics involving both Fe XVII and Fe XVIII.

instrument in its 94 Å imaging channel. The AIA 94 Å channel is multithermal, but in active region core conditions its signal is dominated by the Fe XVIII 93.93 Å line (e.g., O'Dwyer et al. 2010; Warren et al. 2012; Del Zanna 2013a; Petralia et al. 2014; Brooks & Warren 2016). The other contributions to this channel, including those at warm coronal temperatures (1–2 MK); as well as the continuum, which is dependent on both temperature and abundances, are discussed in Del Zanna (2013a). The continuum typically contributes 10–20% to the observed signal. The response of the 94 Å channel of AIA was previously found to be relatively stable over time (Boerner et al. 2014). If this stability continues to hold, and if an active region core is observed, the 94 Å channel of AIA can in principle be used as a proxy for the intensity of the Fe XVIII 93.93 Å line with a sufficient accuracy ($\approx$10%, depending on the continuum, Del Zanna 2013a).

The line intensity ratio of the 93.93 Å line with respect to X-ray lines of Fe XVIII is both sensitive to temperature and κ. Many combinations yield good diagnostic options. Two exam-

ples are shown in the top row of Fig. 7. The ratios to be preferred are those that involve the strong X-ray lines of Fe XVIII (see Sect. 4.2.2), that is, the lines at 14.20, 15.62, 15.83+15.87, and 17.62 Å. The general behavior is such that the sensitivity to κ is strongest at low T, where it can reach $\approx$30% of difference between $\kappa = 2$ and Maxwellian at $\log(T\,[K]) = 6.6$.

Much larger sensitivity to κ can be obtained if the Fe XVIII 93.93 Å line is combined with X-ray lines of both Fe XVII and Fe XVIII, to take advantage of the behavior of the ionization equilibrium with κ. Examples of such diagnostics are shown in the bottom row of Fig. 7. The sensitivity reached in these cases can be as much as a factor of $\approx$3 or larger at $\log(T\,[K]) = 6.6$. The ratio–ratio diagram involving the Fe XVII 15.01 Å/Fe XVIII 93.93 Å–Fe XVIII 93.93 Å/Fe XVIII 14.20 Å sbl has both large sensitivity to T and κ, involves only strong lines, and in good conditions could be used to detect also moderate departures from the Maxwellian. For example, the difference between $\kappa = 5$ and the Maxwellian is still a factor of $\approx$2 at $\log(T\,[K]) = 6.6$.
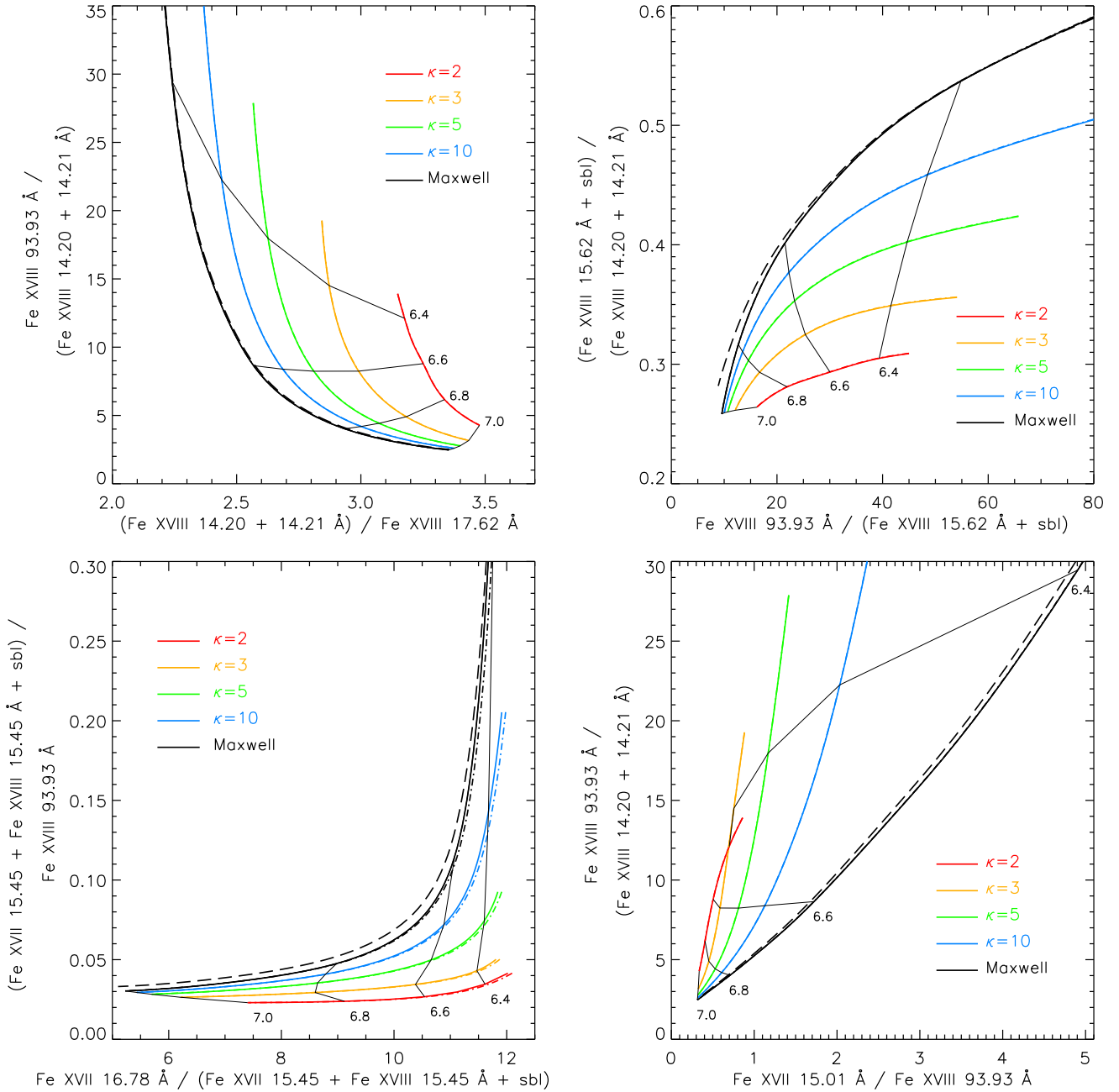
Fig. 7. Same as Fig. 4, but for diagnostics using the MaGIXS X-ray lines in combination with the Fe xviii 93.93 Å line observed by SDO/AIA.

Similar sensitivity is also provided by another of the combinations shown, that of Fe xvii 16.78 Å/Fe xvii 15.45 Å (bl Fe xviii) – Fe xvii 15.45 Å (bl Fe xviii)/Fe xviii 93.93 Å.

4.3. Diagnostics in the multithermal case

The diagnostics presented in Sect. 4 works well for plasma that is isothermal (i.e., at single T) and described by a κ-distribution. However, in many instances, the plasma in active region cores can be multithermal (e.g., Warren et al. 2012; Parenti et al. 2017). The emerging intensity (Eq. (3)) is then given by the expression

$$I_{ji} = \int A_X G_{X,ji}(T, N_e, \kappa) \mathrm{DEM}_\kappa(T)\mathrm{d}T, \qquad (5)$$

where the quantity $\mathrm{DEM}_\kappa(T) = N_e N_H \mathrm{d}l/\mathrm{d}T$ is the differential emission measure (Mason & Monsignori Fossi 1994; Phillips et al. 2008). We note that the concept of DEM and the inversion

of Eq. (5) can be easily extended for the case of κ-distributions (Mackovjak et al. 2014; Dudík et al. 2015; Dzifčáková et al. 2018) simply by using the contribution functions $G(T, N_e, \kappa)$ for the corresponding value of κ.

For the case of active region cores, the DEM_κ constructed for the κ-distributions were found to have similar shapes than the Maxwellian ones: Mackovjak et al. (2014) found that while the peak of the DEM_κ is shifted toward higher T due to the behavior of the ionization equilibrium (Dzifčáková & Dudík 2013), the power-law slope at lower temperatures is nearly the same independently of κ. The slope of the DEM_κ at higher temperatures did change with κ, but there were only a few lines available to constrain it (Mackovjak et al. 2014, Table 1 and Figs. 2–4 therein). The MaGIXS observations, which contain many high-temperature lines, can be helpful in this regard.

In case the DEM has a pronounced high-T shoulder, the Fe xviii lines can be contaminated by blends with Fe xix (cf.,

Parkinson 1975), although in quiescent active region cores the SMM/FCS observations at the same wavelengths showed negligible Fe xviii and no Fe xix (Del Zanna & Mason 2014). The existence Fe xix emission was however observed in active region core conditions in some cases (e.g., Parenti et al. 2017). Thus, the DEM analysis should be performed for the regions observed by MaGIXS, for example by using the hotter lines present in the MaGIXS spectral channel of 6–24 Å. This instrument is well-suited for such analysis, since its spectral band contains lines such as O vii–O viii, Ne ix–Ne x, Mg xi–Mg xii, and Fe xix–Fe xxiv. Alternatively, the DEM_κ can be obtained using the observations made by SDO/AIA (see, e.g., Hannah & Kontar 2012, 2013; Cheung et al. 2015) or Hinode/EIS (see, e.g., Warren et al. 2012; Del Zanna 2013a; Parenti et al. 2017).

If the observed plasma is multithermal, the theoretical curves within ratio–ratio diagrams must be folded over the respective DEM_κ. This has been performed in previous diagnostics of κ-distributions using this technique (Dudík et al. 2015; Dzifčáková et al. 2018). In essence, the DEM-folding of the ratio–ratio curves is a weighted average, where the weights of individual temperature bins are given by the DEM_κ. Therefore, the observed intensities for a multithermal plasma will always be inside the radius of curvature of the ratio–ratio curves. This is an important effect to take into account, since for majority of cases, the ratio–ratio curves for the κ-distributions are located toward the inside of the radius of curvature of the corresponding Maxwellian curve. The ratio–ratio diagrams involving the 15.45 Å blend of Fe xvii and Fe xviii (Fig. 4 right, Fig. 6 bottom right, and Fig. 7 bottom left) are however an exception: For this case, the ratio–ratio curves for the κ-distributions are outside the radius of curvature of the corresponding Maxwellian case. The ratio–ratio diagrams involving this 15.45 Å blend can thus serve as a independent quick check on whether the plasma is multithermal or not, even without the determination of the corresponding DEM_κ. This is because these ratio–ratio diagrams will yield an apparently different value of κ from all the other ratio–ratio diagrams.

5. Summary

We investigated the influence of the non-Maxwellian κ-distributions on the X-ray spectra of Fe xvii and Fe xviii that shall be observed by the MaGIXS instrument. MaGIXS is an X-ray spectrometer, working at 6–24 Å, to be launched in 2020 on a sounding-rocket by NASA. We chose the κ-distributions, characterized by a power-law, high-energy tail of accelerated electrons, since these distributions have been detected previously in the upper solar atmosphere, from transition region to the corona and flares (e.g., Dudík et al. 2015, 2017b; Battaglia et al. 2015; Dzifčáková et al. 2018; Jeffrey et al. 2018; Polito et al. 2018).

The synthetic Fe xvii–Fe xviii spectra were calculated in ionization equilibrium using the method presented in Paper I, which employs the direct integration of the collision strengths over the κ-distributions. We used atomic data compatible with CHIANTI v8 (Del Zanna et al. 2015b); however, we did not take into account the corrections to the level populations (Gu 2003; Landi et al. 2006) that arise mostly due to contributions from dielectronic recombination. This effect is only a minor one at temperatures corresponding to the active region cores, namely, $\log(T\,[\mathrm{K}]) \approx 6.6$. More importantly, throughout the temperature range analyzed in this work, the changes in the line intensity ratios due to these corrections are much smaller than the changes due to the κ-distributions.

At temperatures typical of an active region core, the X-ray spectrum is dominated by Fe xvii lines. Nevertheless, many of Fe xviii lines could be present and visible if some activity is present, even though their intensities will likely not be larger than 10% of the Fe xvii 15.01 Å in quiescent conditions. We investigated the Fe xvii and Fe xviii line intensity ratios to be observed by MaGIXS for sensitivity to κ and T. The values of both T and κ must be diagnosed simultaneously, since they are both parameters of the electron energy distribution. To do that, we used the ratio–ratio method, where the dependence of one line ratio on another line ratio is evaluated for a range of κ and T. Multiple combinations of line ratios well-suited for diagnostics of κ were found. Typically, the ratio–ratio diagrams involve a ratio of a Fe xvii line to an Fe xviii one, combined with another ratio of two lines formed within a single ion. This type of diagnostics provides sensitivity to κ on the order of several tens of per cent. This should be sufficient to diagnose the departures from a Maxwellian using MaGIXS spectra. Since the Fe xvii–Fe xviii lines are relatively close in wavelength, the uncertainties in line intensities should be dominated by photon noise, and the uncertainty of the absolute calibration should not play a role.

In addition, the sensitivity to both κ and T can be increased if the MaGIXS observations are combined with the observations of the well-known Fe xviii 93.93 Å line, routinely observed in the 94 Å channel of SDO/AIA with a cadence of 12 s. When this line is used, the line intensity ratios can depart from a Maxwellian by a factor of 2–3 or more, if an extremely non-Maxwellian case of $\kappa = 2$ is present. We note that such cases have been typically detected previously in the solar atmosphere. The large sensitivity afforded by a combination of the MaGIXS lines in combination with the AIA 94 Å observations could be more than sufficient to overcome possible difficulties due to cross-calibration of the two instruments.

In summary, the Fe xvii and Fe xviii lines to be observed by the MaGIXS instrument are well-suited for detection of the non-Maxwellian distributions in conditions of active region cores, or even at higher temperatures, such as in microflares. Diagnostics of such non-Maxwellian distributions containing accelerated particles would place important constraints on the heating mechanism of the solar corona, as well as provide direct evidence for its impulsive nature.

References

Arregui, I. 2015, Philos. Trans. R. Soc. London Ser. A, 373, 20140261
Battaglia, M., & Kontar, E. P. 2013, ApJ, 779, 107
Battaglia, M., Motorina, G., & Kontar, E. P. 2015, ApJ, 815, 73
Beiersdorfer, P., Bode, M. P., Ishikawa, Y., & Diaz, F. 2014, ApJ, 793, 99
Beiersdorfer, P., Gu, M. F., Lepson, J., & Desai, P. 2011, in 16th Cambridge Workshop on Cool Stars, Stellar Systems, and the Sun, eds. C. Johns-Krull, M. K. Browning, & A. A. West, ASP Conf. Ser., 448, 787
Bian, N. H., Emslie, A. G., Stackhouse, D. J., & Kontar, E. P. 2014, ApJ, 796, 142
Boerner, P., Edwards, C., Lemen, J., et al. 2012, Sol. Phys., 275, 41

Boerner, P. F., Testa, P., Warren, H., Weber, M. A., & Schrijver, C. J. 2014, Sol. Phys., 289, 2377

Bradshaw, S. J., & Viall, N. M. 2016, ApJ, 821, 63

Bromage, G. E., Fawcett, B. C., & Cowan, R. D. 1977, MNRAS, 178, 599

Brooks, D. H., & Warren, H. P. 2016, ApJ, 820, 63

Brosius, J. W., Davila, J. M., Thomas, R. J., & Monsignori-Fossi, B. C. 1996, ApJS, 106, 143

Bryans, P. 2006, On the Spectral Emission of Non-Maxwellian Plasmas, PhD Thesis (University of Strathclyde)

Cargill, P. J. 2014, ApJ, 784, 49

Cargill, P. J., Vlahos, L., Baumann, G., Drake, J. F., & Nordlund, Å. 2012, Space Sci. Rev., 173, 223

Che, H., & Goldstein, M. L. 2014, ApJ, 795, L38

Cheung, M. C. M., Boerner, P., Schrijver, C. J., et al. 2015, ApJ, 807, 143

Clementson, J., & Beiersdorfer, P. 2013, ApJ, 763, 54

Culhane, J. L., Harra, L. K., James, A. M., et al. 2007, Sol. Phys., 243, 19

De Pontieu, B., Title, A. M., Lemen, J. R., et al. 2014, Sol. Phys., 289, 2733

Del Zanna, G. 2006, A&A, 459, 307

Del Zanna, G. 2011, A&A, 536, A59

Del Zanna, G. 2013a, A&A, 558, A73

Del Zanna, G. 2013b, A&A, 555, A47

Del Zanna, G., & Mason, H. E. 2014, A&A, 565, A14

Del Zanna, G., & Mason, H. E. 2018, Liv. Rev. Sol. Phys., 15, 5

Del Zanna, G., Tripathi, D., Mason, H., Subramanian, S., & O'Dwyer, B. 2015a, A&A, 573, A104

Del Zanna, G., Dere, K. P., Young, P. R., Landi, E., & Mason, H. E. 2015b, A&A, 582, A56

Dere, K. P. 2007, A&A, 466, 771

Dere, K. P., Landi, E., Mason, H. E., Monsignori Fossi, B. C., & Young, P. R. 1997, A&AS, 125, 149

Dere, K. P., Landi, E., Young, P. R., et al. 2009, A&A, 498, 915

Desai, P., Brickhouse, N. S., Drake, J. J., et al. 2005, ApJ, 625, L59

Doron, R., & Behar, E. 2002, ApJ, 574, 518

Drake, J. F., Swisdak, M., & Fermo, R. 2013, ApJ, 763, L5

Dudík, J., Del Zanna, G., Mason, H. E., & Dzifčáková, E. 2014, A&A, 570, A124

Dudík, J., Mackovjak, Š., Dzifčáková, E., et al. 2015, ApJ, 807, 123

Dudík, J., Dzifčáková, E., Meyer-Vernet, N., et al. 2017a, Sol. Phys., 292, 100

Dudík, J., Polito, V., Dzifčáková, E., Del Zanna, G., & Testa, P. 2017b, ApJ, 842, 19

Dzifčáková, E., & Del Zanna, G. 2012, in Hinode-3: The 3rd Hinode Science Meeting, eds. T. Sekii, T. Watanabe, & T. Sakurai, ASP Conf. Ser., 454, 167

Dzifčáková, E., & Dudík, J. 2013, ApJS, 206, 6

Dzifčáková, E., Dudík, J., Kotrč, P., Fárník, F., & Zemanová, A. 2015, ApJS, 217, 14

Dzifčáková, E., Zemanová, A., Dudík, J., & Mackovjak, Š. 2018, ApJ, 853, 158

Fletcher, L., Dennis, B. R., Hudson, H. S., et al. 2011, Space Sci. Rev., 159, 19

Galloway, R. K., Helander, P., MacKinnon, A. L., & Brown, J. C. 2010, A&A, 520, A72

Glesener, L., Krucker, S., & Christe, S. 2016, in Space Telescopes and Instrumentation 2016: Ultraviolet to Gamma Ray, Proc. SPIE, 9905, 99050E

Glesener, L., Krucker, S., Hannah, I. G., et al. 2017, ApJ, 845, 122

Golub, L., Deluca, E., Austin, G., et al. 2007, Sol. Phys., 243, 63

Gordovskyy, M., Browning, P. K., Kontar, E. P., & Bian, N. H. 2014, A&A, 561, A72

Gu, M. F. 2003, ApJ, 582, 1241

Hannah, I. G., & Kontar, E. P. 2012, A&A, 539, A146

Hannah, I. G., & Kontar, E. P. 2013, A&A, 553, A10

Hannah, I. G., Hudson, H. S., Hurford, G. J., & Lin, R. P. 2010, ApJ, 724, 487

Harrison, F. A., Craig, W. W., Christensen, F. E., et al. 2013, ApJ, 770, 103

Hasegawa, A., Mima, K., & Duong-van, M. 1985, Phys. Rev. Lett., 54, 2608

Hutcheon, R. J., Pye, J. P., & Evans, K. D. 1976, MNRAS, 175, 489

Jeffrey, N. L. S., Hahn, M., Savin, D. W., & Fletcher, L. 2018, ApJ, 855, L13

Kašparová, J., & Karlický, M. 2009, A&A, 497, L13

Klimchuk, J. A. 2006, Sol. Phys., 234, 41

Klimchuk, J. A. 2015, Philos. Trans. R. Soc. London Ser. A, 373, 20140256

Kobayashi, K., Cirtain, J., & Golub, L. 2010, in Space Telescopes and Instrumentation 2010, Proc. SPIE, 7732, 773233

Kobayashi, K., Winebarger, A. R., & Savage, S. 2017, SPIE Conf. Ser., 10397, 103971I

Kobayashi, K., Winebarger, A. R., & Savage, S. 2018, SPIE Conf. Ser., 10699, 1069927

Kosugi, T., Matsuzaki, K., Sakao, T., et al. 2007, Sol. Phys., 243, 3

Kuhar, M., Krucker, S., Martínez Oliveros, J. C., et al. 2016, ApJ, 816, 6

Kuhar, M., Krucker, S., Glesener, L., et al. 2018, ApJ, 856, L32

Laming, J. M., & Lepri, S. T. 2007, ApJ, 660, 1642

Landi, E., Del Zanna, G., Young, P. R., et al. 2006, ApJS, 162, 261

Landi, E., Young, P. R., Dere, K. P., Del Zanna, G., & Mason, H. E. 2013, ApJ, 763, 86

Le Chat, G., Issautier, K., Meyer-Vernet, N., et al. 2010, in Twelfth International Solar Wind Conference, eds. M. Maksimovic, et al., AIP Conf. Proc., 1216, 316

Le Chat, G., Issautier, K., Meyer-Vernet, N., & Hoang, S. 2011, Sol. Phys., 271, 141

Lemen, J. R., Title, A. M., Akin, D. J., et al. 2012, Sol. Phys., 275, 17

Li, L. P., Peter, H., Chen, F., & Zhang, J. 2015, A&A, 583, A109

Liang, G. Y., & Badnell, N. R. 2010, A&A, 518, A64

Livadiotis, G. 2015, J. Geophys. Res. (Space Phys.), 120, 1607

Livadiotis, G. 2017, Kappa Distributions: Theory and Applications in Plasmas (AE Amsterdam, Netherlands: Elsevier)

Livadiotis, G., & McComas, D. J. 2009, J. Geophys. Res., 114, A11105

Loulergue, M., & Nussbaumer, H. 1975, A&A, 45, 125

Mackovjak, Š., Dzifčáková, E., & Dudík, J. 2014, A&A, 564, A130

Maksimovic, M., Pierrard, V., & Lemaire, J. F. 1997a, A&A, 324, 725

Maksimovic, M., Pierrard, V., & Riley, P. 1997b, Geophys. Res. Lett., 24, 1151

Marsch, E., Rosenbauer, H., Schwenn, R., Muehlhaeuser, K.-H., & Neubauer, F. M. 1982a, J. Geophys. Res., 87, 35

Marsch, E., Schwenn, R., Rosenbauer, H., et al. 1982b, J. Geophys. Res., 87, 52

Marsh, A. J., Smith, D. M., Glesener, L., et al. 2017, ApJ, 849, 131

Mason, H. E., & Monsignori Fossi, B. C. 1994, A&ARv, 6, 123

Meyer-Vernet, N., Moncuquet, M., & Hoang, S. 1995, Icarus, 116, 202

Montag, P., Egedal, J., Lichko, E., & Wetherton, B. 2017, Phys. Plasmas, 24, 062906

Nagata, S., Hara, H., Kano, R., et al. 2003, ApJ, 590, 1095

Nuevo, F. A., Vásquez, A. M., Landi, E., & Frazin, R. 2015, ApJ, 811, 128

O'Dwyer, B., Del Zanna, G., Mason, H. E., Weber, M. A., & Tripathi, D. 2010, A&A, 521, A21

Oka, M., Ishikawa, S., Saint-Hilaire, P., Krucker, S., & Lin, R. P. 2013, ApJ, 764, 6

Oka, M., Krucker, S., Hudson, H. S., & Saint-Hilaire, P. 2015, ApJ, 799, 129

Owocki, S. P., & Scudder, J. D. 1983, ApJ, 270, 758

Parenti, S., del Zanna, G., Petralia, A., et al. 2017, ApJ, 846, 25

Parkinson, J. H. 1973, A&A, 24, 215

Parkinson, J. H. 1975, Sol. Phys., 42, 183

Patsourakos, S., & Klimchuk, J. A. 2009, ApJ, 696, 760

Petralia, A., Reale, F., Testa, P., & Del Zanna, G. 2014, A&A, 564, A3

Petrosian, V., & Liu, S. 2004, ApJ, 610, 550

Phillips, K. J. H., Mathioudakis, M., Huenemoerder, D. P., et al. 2001, MNRAS, 325, 1500

Phillips, K. J. H., Feldman, U., & Landi, E. 2008, Ultraviolet and X-ray Spectroscopy of the Solar Atmosphere (Cambridge University Press)

Polito, V., Dudík, J., Kašparová, J., et al. 2018, ApJ, 864, 63

Reale, F. 2010, Liv. Rev. Sol. Phys., 7, 5

Reale, F., McTiernan, J. M., & Testa, P. 2009a, ApJ, 704, L58

Reale, F., Testa, P., Klimchuk, J. A., & Parenti, S. 2009b, ApJ, 698, 756

Saba, J. L. R., & Strong, K. T. 1991, ApJ, 375, 789

Schmelz, J. T., & Winebarger, A. R. 2015, Philos. Trans. R. Soc. London Ser. A, 373, 20140257

Schmelz, J. T., Kashyap, V. L., Saar, S. H., et al. 2009a, ApJ, 704, 863

Schmelz, J. T., Saar, S. H., DeLuca, E. E., et al. 2009b, ApJ, 693, L131

Schmelz, J. T., Asgari-Targhi, M., Christian, G. M., Dhaliwal, R. S., & Pathak, S. 2015, ApJ, 806, 232

Scudder, J. D., & Karimabadi, H. 2013, ApJ, 770, 26

Seely, J. F., Feldman, U., & Doschek, G. A. 1987, ApJ, 319, 541

Simões, P. J. A., Graham, D. R., & Fletcher, L. 2015, Sol. Phys., 290, 3573

Smith, R. K., & Hughes, J. P. 2010, ApJ, 718, 583

Teriaca, L., Warren, H. P., & Curdt, W. 2012, ApJ, 754, L40

Testa, P., & Reale, F. 2012, ApJ, 750, L10

Ugarte-Urra, I., Warren, H. P., Upton, L. A., & Young, P. R. 2017, ApJ, 846, 165

Veronig, A. M., Rybák, J., Gömöry, P., et al. 2010, ApJ, 719, 655

Vocks, C., Mann, G., & Rausche, G. 2008, A&A, 480, 527

Vocks, C., Dzifčáková, E., & Mann, G. 2016, A&A, 596, A41

Walker, Jr., A. B. C., Rugge, H. R., & Weiss, K. 1974, ApJ, 194, 471

Warren, H. P., Brooks, D. H., & Winebarger, A. R. 2011, ApJ, 734, 90

Warren, H. P., Winebarger, A. R., & Brooks, D. H. 2012, ApJ, 759, 141

Winebarger, A. R., Schmelz, J. T., Warren, H. P., Saar, S. H., & Kashyap, V. L. 2011, ApJ, 740, 2

Winebarger, A. R., Warren, H. P., Schmelz, J. T., et al. 2012, ApJ, 746, L17

Woods, T. N., Eparvier, F. G., Hock, R., et al. 2012, Sol. Phys., 275, 115

Wood, B. E., Laming, J. M., Warren, H. P., & Poppenhaeger, K. 2018, ApJ, 862, 66

Wright, P. J., Hannah, I. G., Grefenstette, B. W., et al. 2017, ApJ, 844, 132

Appendix A: Selected transitions

A list of the spectral lines selected for analysis is provided in Tables A.1 and A.2. Since the calculations outlined in Sect. 3.2 use hundreds of energy levels, resulting in tens of thousands of transitions, we investigated only the lines that are both located in the X-ray portion of the spectrum, and are strong enough to be observed under conditions typical of an active region core. A line is deemed strong enough if its intensity is at least 0.5% of the strongest Fe xvii line, which is the 15.013 Å transition (Parkinson 1973, 1975; Del Zanna 2011).

In addition, the Tables A.1 and A.2 also contain information on the self-blending transitions. A transition is considered a self-blend if it is located within ≲0.3 Å, and its intensity is at least 1% of the primary (strongest) transition. Wavelengths of the primary transition within a selfblend are in Tables A.1 and A.2 given together with the energy levels involved. Selfblending transitions are indicated together with their level numbers. We note that the amount of self-blending transitions is necessarily a function of the wavelength resolution of the spectrometer. Details on the energy levels can be found in Liang & Badnell (2010) for Fe xvii and in Del Zanna (2006) for Fe xviii.

Tables A.1 and A.2 also list possible blending transitions. This list have been compiled by using the CHIANTI database to calculate a spectrum corresponding to the default active region DEM, rather than an isothermal spectrum, to obtain a wider range of blends formed at different temperatures. In addition, the Table I of Parkinson (1975) was reviewed for any possible unidentified lines present in the vicinity. We note that the Tables A.1 and A.2 do not list possible high-temperature blends due to flare lines.

Table A.1. Selected Fe xvii X-ray lines.

λ [Å]	Levels	Level description	I(Max w)	$I(\kappa = 5)$	$I(\kappa = 2)$	Selfblends	Notes
10.504	1–181	$2s^2 2p^6\ ^1S_0 - 2s^2 2p^5 7d\ ^1P_1$	0.0095	0.0106	0.0066	10.494 (1–175)	bl Fe xviii 10.526 Å
10.657	1–165	$2s^2 2p^6\ ^1S_0 - 2s^2 2p^5 6d\ ^3D_1$	0.0089	0.0097	0.0059		bl Fe xix 10.655 Å
10.770	1–155	$2s^2 2p^6\ ^1S_0 - 2s^2 2p^5 6d\ ^1P_1$	0.0159	0.0173	0.0106	10.767 (1–149)	bl Ne ix 10.764 Å, Fe xix 10.816 Å
11.023	1–131	$2s^2 2p^6\ ^1S_0 - 2s^1 2p^6 4p\ ^1P_1$	0.0060	0.0066	0.0044	11.043 (1–129)	bl s Ne ix 11.000 Å, Na x 11.003 Å
11.129	1–118	$2s^2 2p^6\ ^1S_0 - 2s^2 2p^5 5d\ ^3D_1$	0.0328	0.0279	0.0236		bl u 11.160 Å, bl w Na x 11.083 Å
11.250	1–93	$2s^2 2p^6\ ^1S_0 - 2s^2 2p^5 5d\ ^1P_1$	0.0329	0.0343	0.0202	11.264 (1–87) 11.287 (1–85)	bl w Fe xviii 11.253 Å
12.124	1–71	$2s^2 2p^6\ ^1S_0 - 2s^2 2p^5 4d\ ^1P_1$	0.0892	0.0879	0.0496		bl Ne x 12.132 Å, 12.137 Å (Ly-α)
12.264	1–59	$2s^2 2p^6\ ^1S_0 - 2s^2 2p^5 4d\ ^3D_1$	0.0810	0.0791	0.0443		
12.680	1–39	$2s^2 2p^6\ ^1S_0 - 2s^2 2p^5 4s^1\ ^1P_1$	0.0079	0.0067	0.0032		bl Ni xix 12.656 Å bl u 12.75 1Å (Fe xvi d?)
13.159	1–37	$2s^2 2p^6\ ^1S_0 - 2s^1 2p^6 3d\ ^1D_2$	0.0096	0.0089	0.0047		
13.825	1–33	$2s^2 2p^6\ ^1S_0 - 2s^1 2p^6 3p\ ^1P_1$	0.0707	0.0685	0.0392		bl Fe xix 13.844 Å w, bl u 13.868 Å
13.890	1–31	$2s^2 2p^6\ ^1S_0 - 2s^1 2p^6 3p\ ^3P_1$	0.0168	0.0140	0.0066		bl Fe xix 13.872 Å sbl
15.013	1–27	$2s^2 2p^6\ ^1S_0 - 2s^2 2p^5 3d\ ^1P_1$	1.0000	0.8751	0.4452		bl w Fe xix 14.992 Å sbl, bl u 15.050 Å
15.262	1–23	$2s^2 2p^6\ ^1S_0 - 2s^2 2p^5 3d\ ^3D_1$	0.2929	0.2525	0.1259		bl w Fe xvi+Fe xvid sbl 15.27 Å, bl Fe xix 15.208 Å, bl u 15.293Å
15.453	1–17	$2s^2 2p^6\ ^1S_0 - 2s^2 2p^5 3d\ ^3P_1$	0.0615	0.0458	0.0184		bl w Fe xviii 15.397 sbl, 15.450, 15.474, 15.508 Å
16.004	1–14	$2s^2 2p^6\ ^1S_0 - 2s^2 2p^5 3p\ ^1D_2$	0.0166	0.0129	0.0056		bl s O viii 16.006 Å sbl (Ly-β), bl Fe xviii 16.005, 16.026 Å
16.238	1–10	$2s^2 2p^6\ ^1S_0 - 2s^2 2p^5 3p\ ^3P_2$	0.0132	0.0101	0.0043		bl Fe xix 16.272 Å
16.336	1–7	$2s^2 2p^6\ ^1S_0 - 2s^2 2p^5 3p\ ^3D_2$	0.0207	0.0158	0.0066		bl w Fe xix 16.340 Å, w Fe xviii 16.306 Å
16.776	1–5	$2s^2 2p^6\ ^1S_0 - 2s^2 2p^5 3s\ ^3P_1$	0.7304	0.5718	0.2472		
17.051	1–3	$2s^2 2p^6\ ^1S_0 - 2s^2 2p^5 3s\ ^1P_1$	0.9608	0.7450	0.3184		
17.096	1–2	$2s^2 2p^6\ ^1S_0 - 2s^2 2p^5 3s\ ^3P_2$	0.8258	0.6105	0.2418		

Notes. Strongest transitions are listed together with the wavelengths of their selfblends. Intensities relative to the strongest line are listed for the Maxwellian distribution, $\kappa = 5$ and 2, for $\log(T\ [\mathrm{K}]) = 6.6$ and $\log(N_e\ [\mathrm{cm}^{-3}]) = 9$. Possible blending transitions in the vicinity are indicated by "bl". "u" indicates and unidentified transition. "th" denotes that the wavelength is theoretical only. "w" denotes a weak line, while "s" indicates that the line can be stronger than the corresponding Fe xvii one.

Table A.2. Same as for Table A.1, but for Fe xviii.

λ[Å]	Levels	Level description	I(Max w)	I(κ = 5)	I(κ = 2)	Selfblends	Notes
11.3261	1–177	$2s^22p^5\ ^2P_{3/2} - 2s^22p^44d\ ^2D_{5/2}$	0.0051	0.0114	0.0097	11.309 (1–178)	bl Fe xvii 11.287 Å
						11.309 (1–179)	
						11.311 (1–174)	
						11.326 (1–173)	
						11.326 (1–175)	
11.420	1–160	$2s^22p^5\ ^2P_{3/2} - 2s^22p^44d\ ^2D_{5/2}$	0.0048	0.0106	0.0090	11.416 (1–161)	bl Fe xvii 11.420 Å
						11.420 (1–159)	
						11.424 (1–158)	
						11.443 (1–155)	
						11.446 (1–153)	
						11.442 (2–178)	
						11.442 (2–179)	
						11.446 (2–174)	
						11.459 (2–175)	
11.525	1–137	$2s^22p^5\ ^2P_{3/2} - 2s^22p^44d\ ^2F_{5/2}$	0.0053	0.0116	0.0098	11.523 (1–135)	bl s Ne ix 11.547 Å, bl Ni xix 11.539 Å
						11.525 (1–136)	
						11.551 (2–161)	
						11.562 (2–158)	
						11.572 (2–156)	
13.397	1–70	$2s^22p^5\ ^2P_{3/2} - 2s2p^53p\ ^2D_{5/2}$	0.0034	0.0069	0.0057	13.353 (1–71)	
						13.374 (1–72)	
						13.395 (2–80)	
						13.397 (2–79)	
						13.424 (1–69)	
13.962	1–60	$2s^22p^5\ ^2P_{3/2} - 2s^22p^43d\ ^2D_{5/2}$	0.0039	0.0075	0.0055		bl Fe xix 13.938 Å sbl, 14.017 Å
14.144	1–57	$2s^22p^5\ ^2P_{3/2} - 2s^22p^43d\ ^2D_{3/2}$	0.0035	0.0066	0.0047	14.124 (2–62)	
						14.130 (3–108)	
						14.135 (3–107)	
						14.136 (1–58)	
						14.149 (3–105)	
14.204	1–56	$2s^22p^5\ ^2P_{3/2} - 2s^22p^43d\ ^2D_{5/2}$	0.0673	0.1315	0.1002	14.209 (1–55)	
14.258	1–53	$2s^22p^5\ ^2P_{3/2} - 2s^22p^43d\ ^2S_{1/2}$	0.0138	0.0262	0.0192	14.258 (1–52)	
14.373	1–49	$2s^22p^5\ ^2P_{3/2} - 2s^22p^43d\ ^2D_{5/2}$	0.0316	0.0601	0.0442	14.344 (2–58)	
						14.353 (2–57)	
						14.395 (1–48)	
						14.419 (1–47)	
						14.419 (2–55)	
14.487	1–43	$2s^22p^5\ ^2P_{3/2} - 2s^22p^43d\ ^4F_{3/2}$	0.0075	0.0134	0.0090	14.453 (1–46)	bl Ni xx 14.470 Å
						14.470 (2–53)	
						14.477 (1–42)	
						14.487 (1–44)	
14.537	1–41	$2s^22p^5\ ^2P_{3/2} - 2s^22p^43d\ ^2F_{5/2}$	0.0252	0.0470	0.0338	14.551 (1–40)	
						14.580 (1–37)	
						14.580 (3–102)	
14.772	3–98	$2s2p^6\ ^2S_{1/2} - 2s2p^53d\ ^2D_{3/2}$	0.0028	0.0056	0.0042	14.760 (3–97)	bl Fe xix 14.738 Å, O viii 14.821 Å sbl
						14.772 (2–40)	
14.890	2–33	$2s^22p^5\ ^2P_{1/2} - 2s^22p^43d\ ^4D_{3/2}$	0.0042	0.0069	0.0041	14.838 (1–29)	bl Fe xix 14.900 Å
						14.846 (2–38)	
						14.868 (2–34)	
						14.872 (3–89)	
						14.908 (1–28)	
15.397	1–15	$2s^22p^5\ ^2P_{3/2} - 2s^22p^43p\ ^2D_{5/2}$	0.0042	0.0071	0.0044	15.343 (2–24)	bl u 15.372 Å
						15.369 (1–13)	
						15.392 (2–22)	
						15.398 (1–14)	
						15.405 (2–21)	
15.450	3–77	$2s2p^6\ ^2S_{1/2} - 2s2p^53s\ ^2P_{3/2}$	0.0042	0.0073	0.0047	15.439 (2–19)	bl s Fe xvii 15.453 Å
						15.440 (1–11)	
						15.450 (3–78)	
						15.474 (1–12)	
						15.476 (2–17)	
						15.508 (2–20)	
15.622	1–9	$2s^22p^5\ ^2P_{3/2} - 2s^22p^43s\ ^2D_{5/2}$	0.0263	0.0446	0.0281	15.616 (1–10)	
						15.644 (2–15)	
15.766	1–8	$2s^22p^5\ ^2P_{3/2} - 2s^22p^43s\ ^2P_{1/2}$	0.0038	0.0064	0.0040		
15.828	1–7	$2s^22p^5\ ^2P_{3/2} - 2s^22p^43s\ ^4P_{3/2}$	0.0172	0.0285	0.0174		
15.870	2–10	$2s^22p^5\ ^2P_{1/2} - 2s^22p^43s\ ^2D_{3/2}$	0.0178	0.0288	0.0169	15.870 (1–6)	
16.005	1–5	$2s^22p^5\ ^2P_{3/2} - 2s^22p^43s\ ^2P_{3/2}$	0.0335	0.0566	0.0355	16.026 (2–8)	bl s O viii 16.006 Å sbl (Ly-β), bl Fe xvii 16.004 Å
						16.026 (3–65)	
16.072	1–4	$2s^22p^5\ ^2P_{3/2} - 2s^22p^43s\ ^4P_{5/2}$	0.0479	0.0774	0.0450	16.089 (2–7)	in wing of O viii 16.006 Å; bl Fe xix 16.110 Å
16.166	3–64	$2s2p^6\ ^2S_{1/2} - 2s2p^53s\ ^2P_{3/2}$	0.0102	0.0189	0.0129	16.183 (3–63)	
16.306	3–61	$2s2p^6\ ^2S_{1/2} - 2s2p^53s\ ^4P_{3/2}$	0.0033	0.0060	0.0040		bl s Fe xvii 16.336 Å, Fe xix 16.340 Å
17.622	3–29	$2s2p^6\ ^2S_{1/2} - 2s^22p^43p\ ^2P_{3/2}$	0.0260	0.0464	0.0306		
93.932	1–3	$2s^22p^5\ ^2P_{3/2} - 2s2p^6\ ^2S_{1/2}$	0.5790	1.0770	0.8772		SDO/AIA 94 Å passband bl Fe viii, Fe x s, Fe xii s, Fe xiv s, Fe xx, Mg viii see O'Dwyer et al. (2010), Warren et al. (2012) and Del Zanna (2013a)

Notes. The line intensities are scaled with respect to the Fe xvii 15.013 Å line. The 93.93 Å line not observable by MaGIXS is added as well.

Appendix B: Photon noise uncertainties in isothermal Maxwellian and κ = 2 spectra

In Fig. 3, the isothermal spectra at $\log(T\,[\mathrm{K}]) = 6.6$ were presented for the Maxwellian and $\kappa = 2$ distributions. As noted in

Sect. 4.1 and also Appendix A, many of the Fe xviii lines can be weak at these temperatures. To further show the photon noise uncertainties in these weaker lines, the spectra of Fig. 3 are plotted here using a logarithmic intensity axis (Fig. B.1).
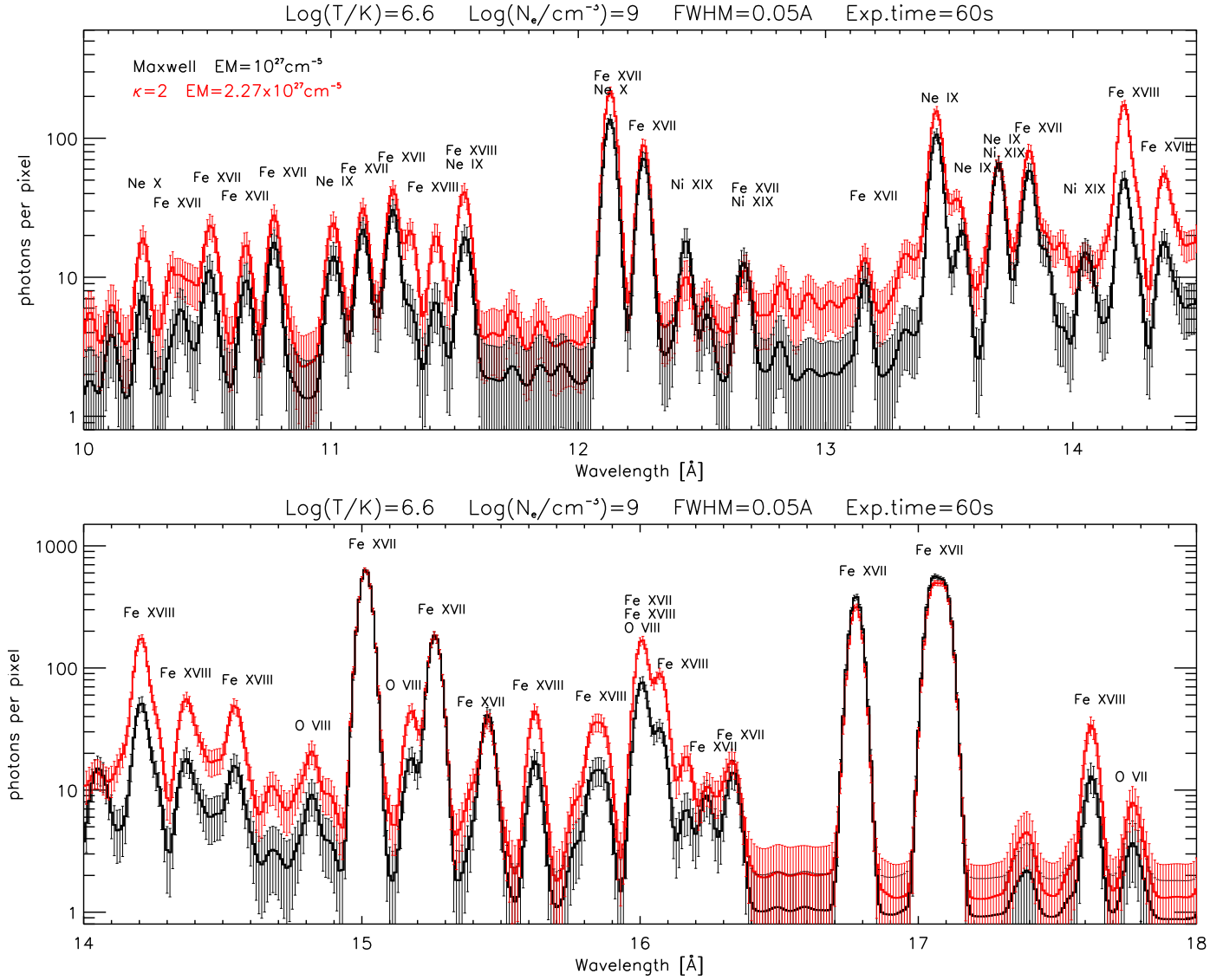

Fig. B.1. Same as Fig. 3, but with logarithmic intensity axis.